Geophysical Research Letters

RESEARCH LETTER
10.1029/2018GL080550

Key Points:
- Dynamic model considering realistic fault geometry and regional stress field reproduces multifault rupture during the Kaikoura earthquake
- Model shows spontaneous rupture arrest on the western Humps and Needles faults, which are unfavorably oriented in a regional stress field
- Dynamic triggering of fault slip may have played an important role in transferring the rupture from the southern to northern faults

Supporting Information:
- Supporting Information S1
- Data Set S1
- Data Set S2

Correspondence to:
R. Ando,
ando@eps.s.u-tokyo.ac.jp

Citation:
Ando, R., & Kaneko, Y. (2018). Dynamic rupture simulation reproduces spontaneous multifault rupture and arrest during the 2016 M_w 7.9 Kaikoura earthquake. *Geophysical Research Letters*, *45*. https://doi.org/10.1029/2018GL080550

Received 20 SEP 2018
Accepted 4 DEC 2018
Accepted article online 10 DEC 2018

Dynamic Rupture Simulation Reproduces Spontaneous Multifault Rupture and Arrest During the 2016 M_w 7.9 Kaikoura Earthquake

Ryosuke Ando[1] **and Yoshihiro Kaneko**[2]

[1]Department of Earth and Planetary Science, School of Science, University of Tokyo, Bunkyō, Tokyo, Japan, [2]GNS Science, Lower Hutt, New Zealand

Abstract The 2016 Kaikoura (New Zealand) earthquake is characterized as one of the most complex multifault rupture events ever observed. We perform dynamic rupture simulations to evaluate to what extent relatively simple forward models accounting for realistic fault geometry can explain the characteristics of coseismic observations. Without fine parameter tuning, our model reproduces many observed features including the multifault rupture, overall slip distribution, and the locations of the maximum slip and rupture arrest. In particular, our model shows spontaneous arrest of dynamic rupture at the both ends of the ruptured fault system due to smaller prestress levels expected from a regional tectonic stress field. Both the simulated and the observationally inferred source time functions show similar double peaks with a larger second peak. The results illuminate the importance of the 3-D fault geometry in understanding the dynamics of complex multifault rupture.

Plain Language Summary The 2016 Kaikoura earthquake in the northern South Island of New Zealand was one of the most complex faulting events ever observed. Previous studies identified surface ruptures along at least a dozen major faults extending over 150 km. Here we use computer simulations to investigate how the complex three-dimensional geometry of faults plays a role in the rupture propagation and termination during the Kaikoura earthquake. We find that our model can explain a number of observations associated with the earthquake. In particular, the model suggests that the termination of propagating rupture at the ends of faults was caused by the unfavorable orientations of these faults with respect to regional tectonic stresses. The results illuminate the importance of three-dimensional fault geometry in understanding the dynamics of multifault earthquakes.

1. Introduction

The 2016 Kaikoura earthquake in the northern South Island of New Zealand was one of the most complex faulting events ever observed. The geometrical complexity of the faults ruptured during the earthquake was captured by field surveys (Clark et al., 2017; Litchfield et al., 2018; Nicol et al., 2018), kinematic inversions using interferometric synthetic aperture radar, and GPS data (Hamling et al., 2017; Xu et al., 2018) and strong motion records (Y. F. Bai et al., 2017; Cesca et al., 2017; Holden et al., 2017; Kaiser et al., 2017; Wang et al., 2018), suggesting that the rupture was initiated near the southwestern end, propagated through a large number of subparallel and conjugate faults extending over 150 km, and terminated at the northeastern end. Although the involvement of the Hikurangi subduction interface is still debated (e.g., Y. F. Bai et al., 2017; Cesca et al., 2017; Holden et al., 2017; Wang et al., 2018; Xu et al., 2018), the source models of the Kaikoura earthquake show heterogeneous slip distributions with the maximum slip on Kekerengu fault (Hamling et al., 2017; Holden et al., 2017; Xu et al., 2018).

While previous studies have provided insights into the kinematics of the Kaikoura earthquake, the physical and tectonic conditions underlying such rupture complexity are poorly understood. In this study, we aim to elucidate the primary factors controlling the observed rupture process by conducting dynamic rupture simulations incorporating a set of basic assumptions while accounting for realistic fault geometry. The model is constrained by seismic and geologic observations prior to the Kaikoura earthquake as much as possible to avoid fine parameter tuning in fitting a range of coseismic observations. We test this dynamic modeling approach and examine how the rupture propagated and arrested during the Kaikoura earthquake.

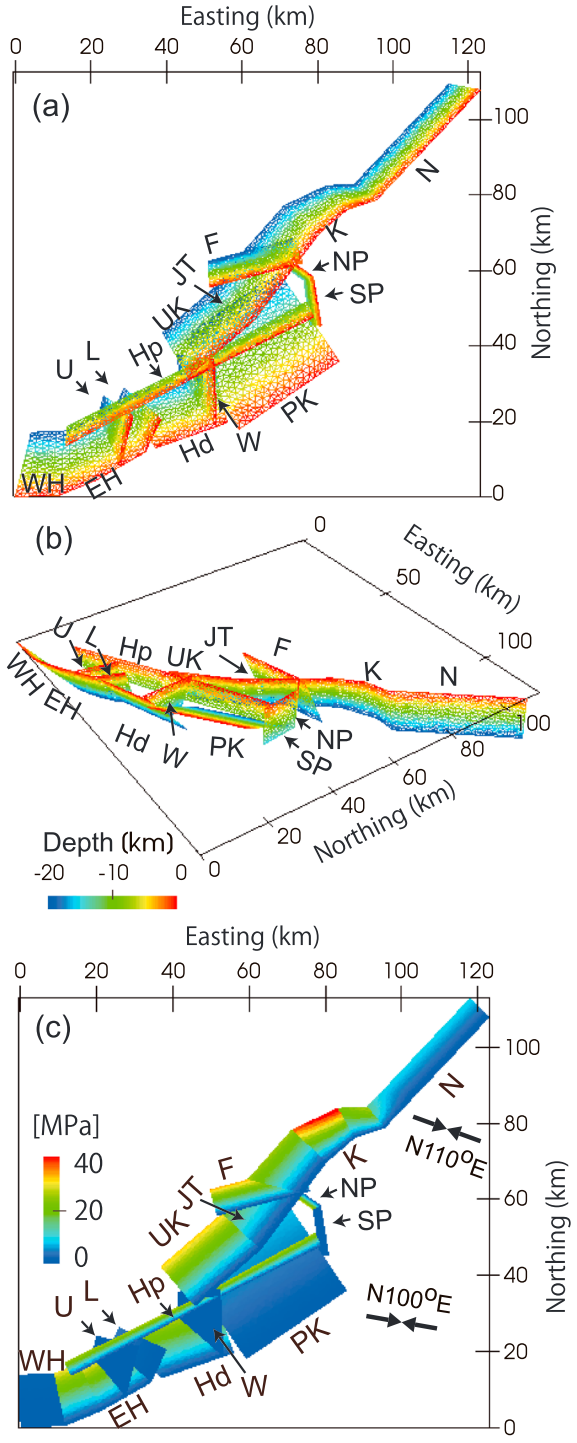

Figure 1. Fault geometry and initial conditions. (a) Map view and (b) perspective view from the southeast. The color corresponds to the depth of the fault surfaces. (c) Spatial distribution of potential stress drop over the fault surfaces. The fault names are abbreviated as follows (the same in the later figures). WH = the western part of the Humps fault, EH = the eastern part of the Humps fault, Hd = the Hundalee fault, W = the Whites fault, PK = the Point Kean fault, U = Unnamed fault, L = the Leaders fault, Hp = the Hope fault, UK = the Upper Kowhai fault, JT = the Jordan Thrust, F = Fidget fault, NP = the northern part of Papatea fault, SP = the southern part of Papatea fault, K = the Kekerengu fault, N = Needles fault.

2. Model and Methods

We employ a fully dynamic rupture simulation using the Fast Domain Partitioning Boundary Integral Equation Method (Ando, 2016; Ando et al., 2017) incorporating frictional fault surfaces embedded into an elastic homogeneous isotropic halfspace. The 3-D fault geometry is considered, given the predominant importance in earthquake rupture dynamics, suggested by field observations (e.g., Stirling et al., 1996), seismic analyses (e.g., Wald & Heaton, 1994), and numerical simulations (e.g., Ando et al., 2017; Aochi & Fukuyama, 2002; Harris & Day, 1999; Oglesby & Mai, 2012). The initial and boundary conditions of the forward model are described by fault geometry, regional tectonic stresses, and fault frictional properties. These parameters are constrained by observations without using inverted slip distributions. We intend to keep our physically based model as simple as possible (except for the fault geometry) in order to constrain the model based on observations prior to the Kaikoura earthquake and to elucidate the key features required to reproduce coseismic observations. Such a model would be testable with available observations.

Fault geometry in the source region can be constrained by previously mapped active fault traces and geological and geomorphological expressions of the subsurface faulting styles (Litchfield et al., 2014). The Kaikoura earthquake broke mostly previously mapped surface fault traces (Litchfield et al., 2018), and interferometric synthetic aperture radar data have been well explained by slip on fault segments with their dip angles fixed to those geologically inferred before the Kaikoura earthquake (Clark et al., 2017; Hamling et al., 2017). Hence, for clarity and objectivity, our modeling assumes the 3-D fault geometry of Clark et al. (2017) with minor modifications to eliminate a few smaller faults and to fill artificial gaps between the original rectangular fault segments (Figure 1). The base depth of the faults is set to be at 20 km (Stirling et al., 2012). To further test possible variations in earthquake scenarios and to evaluate associated physical conditions, our model also includes the Hope fault (Figure 1), which is a major strike-slip fault that was not ruptured during the Kaikoura earthquake, the Papatea fault, which was not included in Clark et al. (2017), and the subduction plate boundary fault.

A regional tectonic stress field is constrained using the results of stress tensor inversions derived from the focal mechanisms of small events (Balfour et al., 2005; Townend et al., 2012). An inferred stress field in the Kaikoura earthquake source region (Townend et al., 2012) shows an east-west compressional strike-slip regime, where the orientation of the maximum principal stress axis slightly rotates by ~10° counterclockwise from N110°E in the northern part to N100°E in the central and southern parts (Figure 1c). Similarly, the stress ratio $\nu = (\sigma_{hmax} - \sigma_v)/(\sigma_{hmax} - \sigma_{hmin}) = 0.66$ is observationally constrained over the focal area (Balfour et al., 2005; Townend et al., 2012), where σ_{hmax}, σ_{hmin}, and σ_s denote the amount of the horizontal maximum, horizontal minimum, and vertical principal stresses, respectively. We further assume that the vertical principal stress σ_v is proportional to the depth z, as observed elsewhere (Brudy et al., 1997), to be the lithostatic minus the hydrostatic overburden pressure given by σ_v/z = 17 MPa/km. The last unknown variable of the regional stresses is constrained by assuming a stress ratio σ_{hmin}/σ_v to satisfy the stress drop being approximately 10 MPa at the hypocenter, consistent with well-established seismological values (e.g., Kanamori & Anderson, 1975).

The constitutive response of the faults is governed by a linear slip-weakening friction law (Ida, 1972) with the coefficients of static and dynamic friction, μ_s and μ_d, and the characteristic slip weakening distance, D_c. Since constraining the spatial distributions of these frictional parameters is quite difficult, uniform distributions are assumed over the fault areas. Hereafter, while we mainly analyze the case of a representative parameter set (referred to Model S) of $\mu_s = 0.35$, $\mu_d = 0.2$ and $D_c = 1.0$ m, and $\sigma_{hmin}/\sigma_v = 0.74$, the neighboring parameter space is also investigated and discussed considering the uncertainties of these parameters (Table S2 in the supporting information). These parameter ranges are broadly consistent with the estimates from laboratory rock experiments (e.g., Di Toro et al., 2004), earthquake source inversions (e.g., Ide & Takeo, 1997), and the average value of $D_c = 2$ m on the Kaikoura earthquake faults inferred from near-fault waveforms (Kaneko et al., 2017).

To initiate the dynamic rupture close to the observationally determined hypocenter (Kaiser et al., 2017), we impose a 3-km-wide circular patch of uniform slip and the corresponding static stress changes on the eastern part of the Humps fault (hereafter the eastern Humps fault), which results in the spontaneous propagation of dynamic rupture outside of the circular patch. Although the actual rupture may have been initiated on an unknown fault a few km south of Humps (Nicol et al., 2018), we assume that the hypocenter is located on the Humps fault. The details of the numerical method (Ando, 2016; Cerjan et al., 1985; Day et al., 2005) and model parameters are described in the supporting information and Tables S1–S3.

3. Results

3.1. Initial Conditions

To identify the main factors that may control the dynamic rupture processes, we first analyze on-fault prestress conditions derived from the regional stress field described above. Figure 1c shows the spatial distribution of potential stress drop on the fault surface, $\delta\tau_o(\boldsymbol{x}) = \tau_o(\boldsymbol{x}) - \mu_d\sigma_o(\boldsymbol{x})$, which is primarily a function of the fault surface orientations and depth, where τ_o and σ_o denote the initial values of the maximum shear tractions and the normal traction on the fault surface at the location $\boldsymbol{x}$. This spatial distribution is objectively determined based on the abovementioned observations without subjective segment-by-segment tuning of the stress and frictional parameters.

By assessing the spatial variation of the potential stress drop $\delta\tau_o$ (Figure 1c), we find that individual fault segments depict striking differences. For example, the Kekerengu fault exhibits the most favorable orientation in the regional stress field and leads to the highest potential stress drop, while the Needles fault and the western part of the Humps fault (hereafter the western Humps fault) are at unfavorable orientations (Figure 1c). These differences can be understood from the angles between the maximum horizontal principal stress and the overall strikes of the fault segments under the strike-slip stress regime. For example, the fault strikes of the Kekerengu fault with respect to the maximum horizontal principal stress axis, ~40°, is much closer to the optimal angle of $\mu_d = 0.2$ than that of the Needles fault, ~70°. The choices of the frictional coefficient have negligible effect because the internal frictional angle only changes by 5° with changing μ_d from 0.2 to 0.4. In addition, the difference of 10° in the assumed principal stress axis (e.g., Klinger et al., 2018) exhibits a qualitatively similar distribution of potential stress drop (Figure S1).

The eastern Humps fault is favorably oriented (Figure 1c). This could explain why the rupture may have easily propagated or jumped to the eastern Humps fault from the actual hypocenter a few kilometers south of the fault (Nicol et al., 2018). The difference between the actual and assumed hypocenters also implies that the current simulation may lack this initial rupture process.

3.2. Dynamic Rupture Process

We next analyze the simulated dynamic rupture process and identify the first-order features to be compared with coseismic observations. Figure 2 and Movie S1 present the spatiotemporal evolutions of the fault slip and the shear and normal traction changes, $\Delta\tau(t)$ and $\Delta\sigma(t)$, described by the dynamic Coulomb Failure stress change $\Delta CFS(t) = \Delta\tau(t) - \mu_s\Delta\sigma(t)$ with time t (Harris, 1998). We first describe the results of the model without the Hope, Papatea, and subduction interface faults; the role of these faults are discussed later.

At time $t = 0$ s (Figure 2, top left), the rupture is nucleated on the eastern Humps fault (arrowed). During the first 20 s, while the rupture initially propagates bilaterally, the rupture propagating toward the west onto the

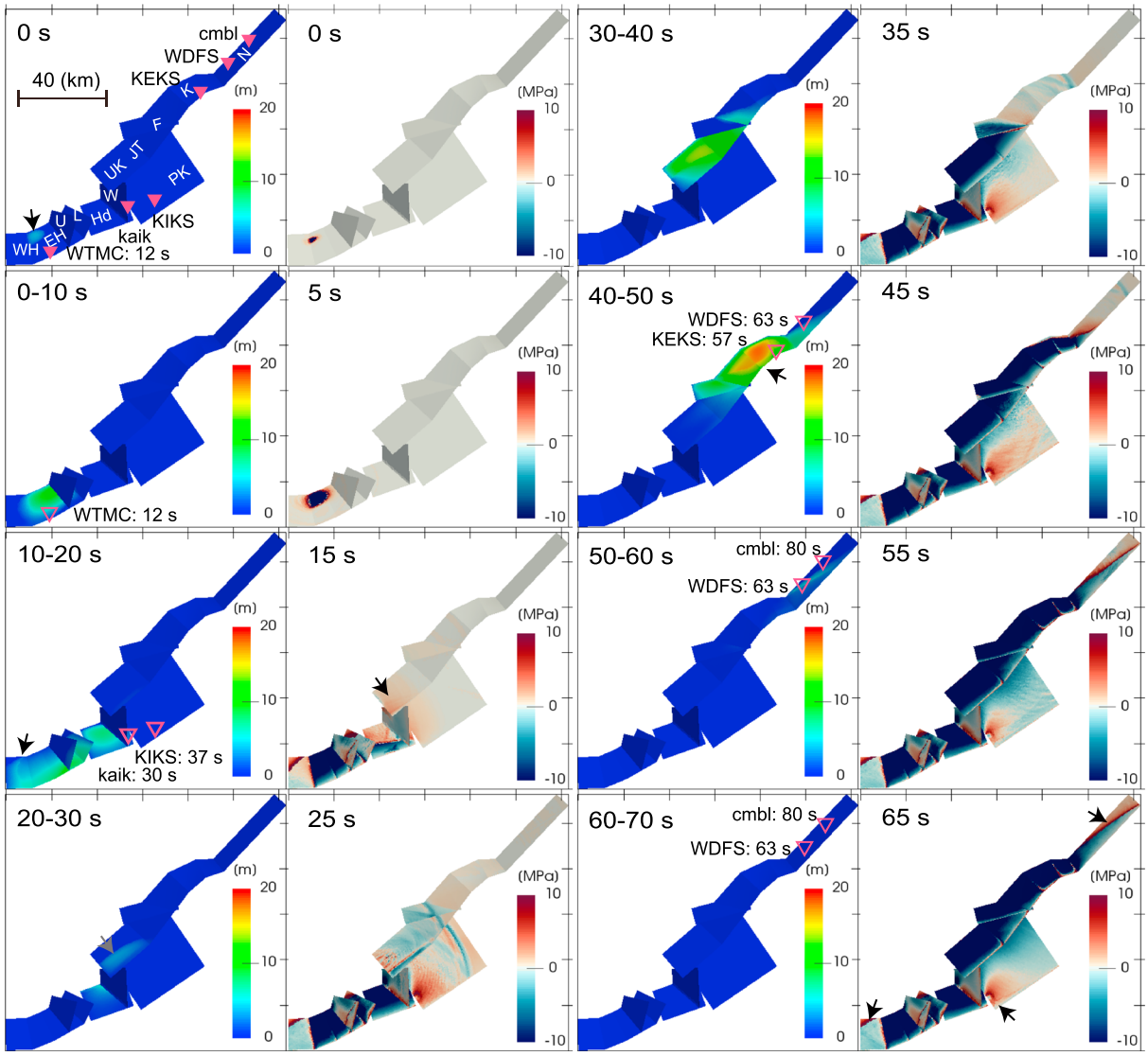

Figure 2. Snapshots of dynamic rupture propagation in Model S. (Left) Slip accumulated in the indicated 10-s intervals. (right) The dynamic Coulomb Failure Stress change (ΔCFS) at the indicated times. The pink triangles denote seismic or high-rate GPS stations shown with the station codes and the recorded timing (seconds after the origin time) of the peak velocity lowpass-filtered at 1 Hz. The average rupture velocity is ~2.5 km/s. The fault names are indicated in the top-left panel (see Figure 1 caption for abbreviation).

western Humps fault is eventually arrested (arrowed to the slip in the 15-s panel). The rupture further propagates toward the east along the eastern Humps fault and then onto the Hundalee fault. The three branching faults (Unnamed, Leaders, and Whites) generally do not exhibit large slip due to their unfavorable fault orientations (Figure 1c). Around that time, a few MPa of positive ΔCFS transfer onto the Upper Kowhai fault (arrowed in the 15-s panel) by the wave radiation from ruptured faults.

Around t = 25 s, the rupture jumps from the Hundalee fault onto the shallower portion of the Upper Kowhai fault (pointed by the gray arrow). Since the rupture hardly propagates through the Whites fault, which connects the Hundalee and the Upper Kowhai faults, the rupture transfer occurs dynamically, and the slip on Upper Kowhai is triggered by the abovementioned transient positive ΔCFS (Figure 2). We confirm that decreasing the poorly constrained dip of the Whites fault do not significantly change the rupture behavior (Movie S2 and Figure 3a, inset). The rupture propagation on the Point Kean fault is limited due to its unfavorable fault orientation (Figure 1c).

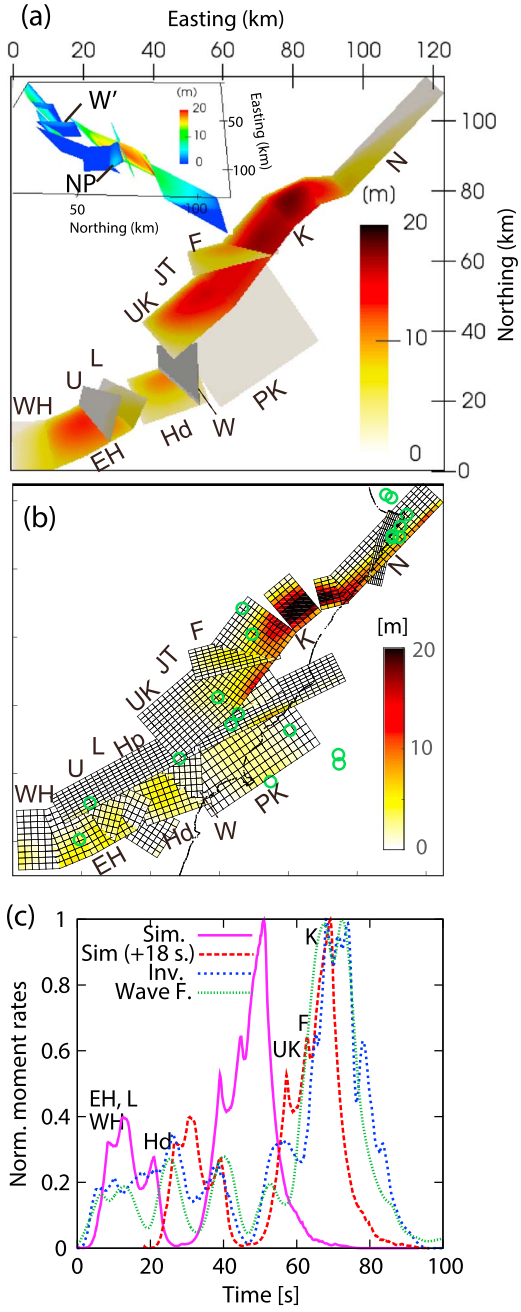

Figure 3. Comparison of simulated coseismic processes with observationally inferred ones. Final slip distributions from (a) dynamic simulation in Model S and (b) the inversion of geodetic data (Clark et al., 2017). The model with the Papatea fault is also shown in the inset of Figure 3a, in the view from the east (NP = the northern part of Papatea fault, W′ = the Whites fault assuming a shallower dip angle). Green circles indicate the epicenters of the aftershocks ($M > 5.5$) from 12 November 2016 to 12 November 2017. Note that minor faults removed from the simulation are presented in Figure 3b. (c) Moment rate functions normalized by the peak values from the dynamic simulation and two kinematic models (Holden et al., 2017). Different curves correspond to moment rate functions from kinematic inversion (blue) and wavefield modeling (green) and the dynamic simulation without (purple) and with (red) the time shift of 18 s. For the dynamic simulation, fault ruptures responsible for the individual peaks are indicated. The moment magnitude is 7.9 for both the dynamic and kinematic models.

To better understand the dynamic triggering of the Upper Kowhai fault, we identify sets of friction and stress parameters signifying a Hopf bifurcation behavior (e.g., Day, 1982; Hirsch & Smale, 1974; Madariaga & Olsen, 2000; see Table S2 for the compilation). Increasing the value of D_c and decreasing the stress drop through σ_{hmin}/σ_v from those in Model S by less than a few percent do not lead to the triggering of slip on Upper Kowhai. Since the dynamic triggering occurs or not is related to a bifurcation point in the solution space in the range of admissible parameter values, these can be regarded as two plausible scenarios, with the former one consistent with the Kaikoura earthquake observation (Holden et al., 2017).

Subsequently, the rupture propagates through Jordan Thrust at t = ~35 s and then the Fidget and Kekerengu faults at ~45 s. It is remarkable that the Kekerengu fault exhibits the maximum slip among all the ruptured faults (Figure 2), as expected from its highest potential stress drop (Figure 1c).

3.3. Spontaneous Arrest of the Dynamic Rupture

Model S shows that the rupture to the northeast eventually slows down on the Needles fault at t = ~55 s and is spontaneously arrested after t = 65 s. The rupture is also spontaneously arrested at the southwest end of the western Humps fault and in the middle on the Point Kean fault. The arrest of the rupture is visible with residual positive ΔCFS localized along the perimeter of the slip areas (arrowed at t = 65 s). While relatively small slip can still occur at shallow depths on these three faults because of the smaller overburden pressure and static frictional strengths there, these faults are unfavorably oriented, resulting in insufficient energy release rate and spontaneous rupture arrest.

3.4. Comparison With Slip Model Derived From Geodetic Data

Figures 3a and 3b show the spatial distribution of final slip in Model S and that from the inversion of geodetic data (Clark et al., 2017; Hamling et al., 2017), respectively. The moment magnitude in Model S is 7.9, consistent with kinematic models (Clark et al., 2017; Hamling et al., 2017; Holden et al., 2017). Varying the stress drop through σ_{hmin}/σ_v affects the magnitude (Table S2) but does not change the spatial pattern of the slip distribution. The simulated slip distribution reproduces the primary features of the observationally estimated one, including the maximum slip on the Kekerengu fault, a smaller amount of slip on the Needles, and the western Humps faults where the rupture is arrested (Figure 3), and predominantly right-lateral with some reverse slip on the ruptured faults (Figure S2). In Model S, the energy-based stress drop (Noda et al., 2013) is 18 MPa, smaller than 30–34 MPa reported for kinematic models of the Kaikoura earthquake (Kaneko et al., 2017; Xu et al., 2018) but still much larger than typical values 1–10 MPa for crustal earthquakes (e.g., Kanamori & Anderson, 1975).

The depth-dependent distribution of slip averaged over all the fault segments appears to be slightly (~3 km) deeper in the simulation than the geodetically derived slip model (Figure 3). The depth of the peak slip would shift shallower if we assume weaker depth-dependence of vertical principal stress inferred from the estimates of stress drops (e.g., Uchide et al., 2014) and smaller rigidity at shallow depths. However, our simulations with different sets of model parameters show that this depth dependence does not affect the along-strike variation of depth-averaged slip, which is a robust feature among different models.

Figure 3b also shows the epicenters of large ($M > 5.5$) aftershocks. Although the spatial correlation between the locations of these aftershocks and the locations of rupture arrest is not obvious, a prominent aftershock cluster located near the northern end of the Needles fault may have been caused by large stress loading associated with the rupture arrest (Figure 2, $t = 65$ s).

3.5. Comparison of the Temporal Evolution of the Rupture in the Simulation With Observations and Kinematic Source Models

We compare simulated rupture arrival times with the timing of the peak ground velocity (PGV) recorded at stations in the vicinity of ruptured faults. Figure 2 shows the locations of nearfield seismic and high-rate sampling GPS stations together with the timing of the recorded PGV low-pass filtered at 1 Hz. Because these stations are close (<10 km) to the ruptured faults, we can assume that the observed PGVs are predominantly generated by the propagating fault slip passing by the vicinity of the stations, and the same goes for the timings.

Station WTMC located closed to the surface trace of the eastern Humps fault shows the PGV at 12 s after the origin time (Figure 2), suggesting that the actual initial rupture process was quite slow on the eastern Humps fault, or perhaps slip on the eastern Humps fault was triggered by earlier rupturing of another fault located at a few kilometer south of it (e.g., Kaiser et al., 2017), which is not considered in this study. The observed difference between the PGV times at stations WTMC and kaik (separated by ~40 km) is 18 s; the corresponding time difference in the simulation is 15 s (Figure 2). Station KEKS recorded the PGV time at 57 s, which is ~15 s behind the simulated rupture on the Kekerengu fault, consistent with the time difference of the rupture arrival in the earlier stage (Figure 2). The PGV time difference between stations WDFS and cmbl (separated by ~20 km) is 17 s, and hence, the rupture propagation there must have been quite slow, consistent with the simulated gradual rupture arrest on the Needles fault (Figure 2).

Next, we compare a simulated moment rate function (MRF) to those previously derived from kinematic slip inversion and wavefield modeling (Holden et al. (2017; Figure 3c). A common feature in these MRFs is the group of the earlier small peaks followed by a larger peak. In the simulation, the former corresponds to rupturing the eastern and western Humps faults, the Leaders and Hundalee faults, and the latter is rupturing the Upper Kowhai fault to the Needles fault, where the Fidget fault contributes to the middle peak appearing ~6 s before the largest peak generated by the Kekerengu fault. Holden et al. (2017) explained the origin of their observationally identified peaks with similar grouping of the fault segments. If the rupture process between these earlier and later stages were more continuous, the MRFs would have become more continuous without such distinct early and late peaks, implying the occurrence of the dynamic triggering process between them.

At the same time, the simulated total duration of MRF is shorter than those observationally inferred (Figure 3c). We find that shifting the simulated MRF by 18 s (red curve in Figure 3c) leads to a reasonable agreement in the overall shape, suggesting that the actual rupture process in the earlier stage is longer than the simulated one. Hence, it is speculated that the longer duration may be explained by a dynamic model with more irregular fault geometries of the Humps and Hundalee faults than what is currently assumed and/or may be due to the abovementioned more complex rupture nucleation south of the Humps fault. For the later stage, the simulated MRF with the time shift (red curve in Figure 3c) still underestimates the observationally inferred prolonged duration, which is interpreted as the delayed onset of rupture at the deeper potion of the Kekerengu fault (Holden et al., 2017). This issue remains a subject of future study.

4. Discussion

4.1. The Pattern of Multifault Rupture

Our forward modeling shows that this spatial variation seen in the observation (Clark et al., 2017; Hamling et al., 2017) can be well explained by the effect of the geometrical variations of this nonplanar fault system. This result is remarkable in that unlike many of previous studies on dynamic rupture simulations, our model does not need to assume an artificial barrier for the rupture arrest. While the idea that unfavorably oriented faults serve as the termination of a spontaneously propagating rupture has been previously proposed via kinematic analysis of large earthquakes (e.g., Bouchon et al., 1998), we demonstrate, using dynamic rupture modeling, that such idea can explain the rupture arrest of a complex multifault earthquake.

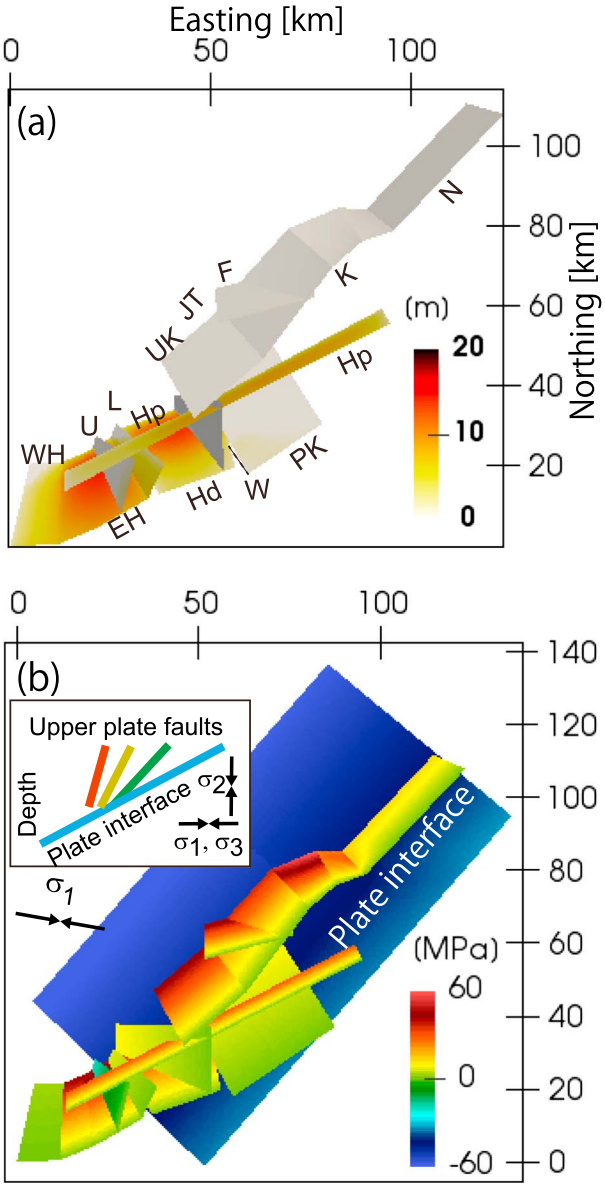

Figure 4. Geometrical model variations. (a) Final slip distributions of the model that includes the Hope fault. (b) Potential stress drop distribution for the model that includes the plate interface, which dips 12° to the northwest and is located just underneath the crustal faults (Hamling et al., 2017). (inset) Schematic sectional view of upper-plate faults and plate boundary fault.

Connecting faults in the south, particularly the Whites fault, do not exhibit significant slip (Figure 3a). This suggests that rupturing the Whites fault may not be the main mechanism that caused the rupture transferring from the Hundalee fault in the south to the Upper Kowhai fault in the north with the minimum separation distance of 13 km. Rather, transient dynamic stresses or the elastic waves would have played the main role in the rupture jumping over 13 km from the southern to the northern fault segments. Such unusually large rupture jump may have been attributed to the large seismogenic width (20 km; K. Bai & Ampuero, 2017). Similar argument can be made to understand the role of the Papatea fault in transferring the rupture from the southern to northern fault segments. Although the northern part of the Papatea fault is favorably oriented and generates slip, its southern part connecting the Point Kean fault in the south to the Kekerengu fault in the north is unfavorable, as shown in the map of the potential stress drop (Figure 1c) and the corresponding simulation (Figure 3a, inset, and Movie S2). Hence, our model implies that the Papatea fault did not play a dominant role in the rupture transfer from the southern to the northern fault segments. Note that slip on the northern part of the Papatea fault may have been enhanced by rigid-block rotation as suggested by Hamling et al. (2017).

Predicting the locations of rupture arrest is important for estimating earthquake sizes for seismic hazard assessment. Such prediction is a difficult problem, particularly for planar fault models where rupture arrest is often assumed to be due to heterogeneous distributions of stress and strength (e.g., Miyatake, 1992). Although obtaining good preseismic estimates of these fault properties is fundamentally difficult, we note that our simple forward model successfully reproduces the actual rupture arrest locations.

4.2. Role of the Hope Fault

The Hope fault, which had been considered as the most active fault in the source region, led to significantly smaller amount of slip compared to nearby fault segments (Hundalee and Humps) running parallel to it (Hamling et al., 2017). Since the orientation of the Hope fault is favorable to the regional stress field (Figure 1c), we would expect the Hope fault to have been ruptured during the Kaikoura earthquake. Our simulation with the Hope fault (Figure 4a) indeed shows that the rupture jumps from the Humps and Hundalee faults to the Hope fault that produces ~~10 m of slip, which was not observed (Hamling et al., 2017). Interestingly, the rupturing of the Hope fault also prevents the rupture propagation onto the Upper Kowhai fault in the north (Figure 4a).

Since our model assumes relatively simple tectonic stress state on all the faults without considering the histories of previous major earthquakes, our results indicate that the shear stress on this section of the Hope fault was not high enough at the time of the Kaikoura earthquake. This implies the presence of second-order stress heterogeneity in addition to the first-order regional stress field. Such an inference is consistent with the paleoseimological observation that the Hope fault was ruptured by the 1888 Amuri earthquake or the 1780 M>7 earthquake and may not have been fully reloaded at the time of the Kaikoura earthquake, given the estimated mean recurrence interval of 180–310 years (Langridge et al., 2003). Further examinations will be the subject of future studies.

4.3. Role of the Hikurangi Subduction Interface

An extension of the current model to include the subduction interface may provide a clue to understand its involvement during the Kaikoura earthquake. Since seismicity used to constrain the regional stress field covers the depth range of the subduction interface (Townend et al., 2012), we use subduction interface

geometry considered in Hamling et al. (2017) and analyze the prestress state (Figure 4b). The calculated potential stress drops on the subduction interface show negative values due to its unfavorable shallow dip angle under the strike-slip regime, rendering it unable to generate spontaneous coseismic slip in a wide area. While the rupture penetrating onto the subduction interface is still possible, our analysis indicates that large (>10 m) coseismic slip in a wide area is unlikely, implying a minor contribution of the subduction interface to the overall seismic moment. More detailed analyses on stress states at depths will provide further constraints on this issue.

5. Conclusions

The rupture process of the complex Kaikoura earthquake is reasonably well reproduced by forward dynamic model incorporating realistic 3D fault geometry and regional stress field. The reproduced features include rupture transfer across multiple fault segments and the spontaneous arrest of the rupture at the northeastern end of the Needles fault and the southwestern Humps fault. The spontaneous rupture arrest is caused by smaller prestress levels on these faults expected from regional stress field. The simulated slip distribution with the maximum slip on the Kekerengu fault is also in good agreement with geodetically and seismically derived slip models. Dynamic triggering of fault slip may have played an important role in transferring the rupture from the southern to northern fault segments. These results highlight the importance of the 3D fault geometry in understanding the dynamics of complex multifault rupture.

Acknowledgments
This study is supported in part by JSPS/MEXT KAKENHI grants JP25800253 and JP26109007, by the "Joint Usage/Research Center for Interdisciplinary Large-scale Information Infrastructures" and "High Performance Computing Infrastructure" in Japan (Project ID: jh170017-NAH), Rutherford Discovery Fellowship, and public funding from the Government of New Zealand. We thank I. Hamling for providing the fault geometry data and fruitful discussions. We also thank Editor Gavin Hayes, Associate Editor, Ruth Harris, and an anonymous reviewer for their comments that helped us improve the article. Numerical data used for generating figures and movies in this paper are available at http://www-solid.eps.s.u-tokyo.ac.jp/~ando/data/18kaikoura.

References

Ando, R. (2016). Fast domain partitioning method for dynamic boundary integral equations applicable to non-planar faults dipping in 3-D elastic half-space. *Geophysical Journal International*, *207*(2), 833–847. https://doi.org/10.1093/gji/ggw299

Ando, R., Imanishi, K., Panayotopoulos, Y., & Kobayashi, T. (2017). Dynamic rupture propagation on geometrically complex fault with along-strike variation of fault maturity: Insights from the 2014 northern Nagano earthquake. *Earth, Planets and Space*, *69*(1). https://doi.org/10.1186/s40623-017-0715-2

Aochi, H., & Fukuyama, E. (2002). Three-dimensional nonplanar simulation of the 1992 Landers earthquake. *Journal of Geophysical Research*, *107*(B2), 2035. https://doi.org/10.1029/2000JB000061

Bai, K., & Ampuero, J. P. (2017). Effect of seismogenic depth and background stress on physical limits of earthquake rupture across fault step overs. *Journal of Geophysical Research: Solid Earth*, *122*, 10,280–10,298. https://doi.org/10.1002/2017JB014848

Bai, Y. F., Lay, T., Cheung, K. F., & Ye, L. L. (2017). Two regions of seafloor deformation generated the tsunami for the 13 November 2016, Kaikoura, New Zealand earthquake. *Geophysical Research Letters*, *44*, 6597–6606. https://doi.org/10.1002/2017GL073717

Balfour, N. J., Savage, M. K., & Townend, J. (2005). Stress and crustal anisotropy in Marlborough, New Zealand: Evidence for low fault strength and structure-controlled anisotropy. *Geophysical Journal International*, *163*(3), 1073–1086. https://doi.org/10.1111/j.1365-246X.2005.02783.x

Bouchon, M., Campillo, M., & Cotton, F. (1998). Stress field associated with the rupture of the 1992 Landers, California, earthquake and its implications concerning the fault strength at the onset of the earthquake. *Journal of Geophysical Research*, *103*, 21,091–21,097. https://doi.org/10.1029/98JB01982

Brudy, M., Zoback, M. D., Fuchs, K., Rummel, F., & Baumgartner, J. (1997). Estimation of the complete stress tensor to 8 km depth in the KTB scientific drill holes: Implications for crustal strength. *Journal of Geophysical Research*, *102*, 18,453–18,475. https://doi.org/10.1029/96JB02942

Cerjan, C., Kosloff, D., Kosloff, R., & Reshef, M. (1985). A nonreflecting boundary-condition for discrete acoustic and elastic wave-equations. *Geophysics*, *50*(4), 705–708. https://doi.org/10.1190/1.1441945

Cesca, S., Zhang, Y., Mouslopoulou, V., Wang, R., Saul, J., Savage, M., et al. (2017). Complex rupture process of the M_w 7.8, 2016, Kaikoura earthquake, New Zealand, and its aftershock sequence. *Earth and Planetary Science Letters*, *478*, 110–120. https://doi.org/10.1016/j.epsl.2017.08.024

Clark, K. J., Nissen, E. K., Howarth, J. D., Hamling, I. J., Mountjoy, J. J., Ries, W. F., et al. (2017). Highly variable coastal deformation in the 2016 M_W7.8 Kaikoura earthquake reflects rupture complexity along a transpressional plate boundary. *Earth and Planetary Science Letters*, *474*, 334–344. https://doi.org/10.1016/j.epsl.2017.06.048

Day, S. M. (1982). 3-dimensional simulation of spontaneous rupture—The effect of nonuniform prestress. *Bulletin of the Seismological Society of America*, *72*(6), 1881–1902.

Day, S. M., Dalguer, L. A., Lapusta, N., & Liu, Y. (2005). Comparison of finite difference and boundary integral solutions to three-dimensional spontaneous rupture. *Journal of Geophysical Research*, *110*, B12307. https://doi.org/10.1029/2005JB003813

Di Toro, G., Goldsby, D. L., & Tullis, T. E. (2004). Friction falls towards zero in quartz rock as slip velocity approaches seismic rates. *Nature*, *427*(6973), 436–439. https://doi.org/10.1038/nature02249

Hamling, I. J., Hreinsdóttir, S., Clark, K., Elliott, J., Liang, C., Fielding, E., et al. (2017). Complex multifault rupture during the 2016 M_w 7.8 Kaikoura earthquake, New Zealand. *Science*, *356*(6334). https://doi.org/10.1126/science.aam7194

Harris, R. A. (1998). Introduction to special section: Stress triggers, stress shadows, and implications for seismic hazard. *Journal of Geophysical Research*, *103*, 24,347–24,358. https://doi.org/10.1029/98JB01576

Harris, R. A., & Day, S. M. (1999). Dynamic 3D simulations of earthquakes on en echelon faults. *Geophysical Research Letters*, *26*, 2089–2092. https://doi.org/10.1029/1999GL900377

Hirsch, M. W., & Smale, S. (1974). *Differential equations, dynamical systems, and linear algebra* (p. 358). San Diego, CA: Academic Press.

Holden, C., Kaneko, Y., D'Anastasio, E., Benites, R., Fry, B., & Hamling, I. J. (2017). The 2016 Kaikoura earthquake revealed by kinematic source inversion and seismic wavefield simulations: Slow rupture propagation on a geometrically complex crustal fault network. *Geophysical Research Letters*, *44*, 11,320–11,328. https://doi.org/10.1002/2017GL075301

Ida, Y. (1972). Cohesive force across the tip of a longitudinal-shear crack and Griffith's specific surface energy. *Journal of Geophysical Research*, *77*, 3796–3805. https://doi.org/10.1029/JB077i020p03796

Ide, S., & Takeo, M. (1997). Determination of constitutive relations of fault slip based on seismic wave analysis. *Journal of Geophysical Research*, *102*, 27,379–27,391. https://doi.org/10.1029/97JB02675

Kaiser, A., Balfour, N., Fry, B., Holden, C., Litchfield, N., Gerstenberger, M., et al. (2017). The 2016 Kaikoura, New Zealand, earthquake: Preliminary seismological report. *Seismological Research Letters*, *88*(3), 727–739. https://doi.org/10.1785/0220170018

Kanamori, H., & Anderson, D. L. (1975). Theoretical basis of some empirical relations in seismology. *Bulletin of the Seismological Society of America*, *65*(5), 1073–1095.

Kaneko, Y., Fukuyama, E., & Hamling, I. J. (2017). Slip-weakening distance and energy budget inferred from near-fault ground deformation during the 2016 M_w7.8 Kaikura earthquake. *Geophysical Research Letters*, *44*, 4765–4773. https://doi.org/10.1002/2017GL073681

Klinger, Y., Okubo, K., Vallage, A., Champenois, J., Delorme, A., Rougier, E., et al. (2018). Earthquake damage patterns resolve complex rupture processes. *Geophysical Research Letters*, *45*, 10,279–210,287. https://doi.org/10.1029/2018GL078842

Langridge, R., Campbell, J., Hill, N., Pere, V., Pope, J., Pettinga, J., et al. (2003). Paleoseismology and slip rate of the Conway Segment of the Hope Fault at Greenburn Stream, South Island, New Zealand. *Ann Geophys-Italy*, *46*(5), 1119–1139.

Litchfield, N. J., van Dissen, R., Sutherland, R., Barnes, P. M., Cox, S. C., Norris, R., et al. (2014). A model of active faulting in New Zealand. *New Zeal J Geol Geop*, *57*(1), 32–56. https://doi.org/10.1080/00288306.2013.854256

Litchfield, N. J., Villamor, P., van Dissen, R., Nicol, A., Barnes, P. M., Barrell, D. J. A., et al. (2018). Surface rupture of multiple crustal faults in the 2016 M_w 7.8 Kaikōura, New Zealand, earthquake. *Bulletin of the Seismological Society of America*, *108*(3b), 1496–1520. https://doi.org/10.1785/0120170300

Madariaga, R., & Olsen, K. B. (2000). Criticality of rupture dynamics in 3-D. *Pure and Applied Geophysics*, *157*(11), 1981–2001. https://doi.org/10.1007/PL00001071

Miyatake, T. (1992). Dynamic rupture processes of inland earthquakes in Japan weak and strong asperities. *Geophysical Research Letters*, *19*, 1041–1044. https://doi.org/10.1029/92GL01046

Nicol, A., Khajavi, N., Pettinga, J., Fenton, C., Stahl, T., Bannister, S., et al. (2018). Preliminary geometry, displacement, and kinematics of fault ruptures in the epicentral region of the 2016 M_w 7.8 Kaikōura, New Zealand, earthquake. *Bulletin of the Seismological Society of America*, *108*(3B), 1521–1539. https://doi.org/10.1785/0120170329

Noda, H., Lapusta, N., & Kanamori, H. (2013). Comparison of average stress drop measures for ruptures with heterogeneous stress change and implications for earthquake physics. *Geophysical Journal International*, *193*(3), 1691–1712. https://doi.org/10.1093/gji/ggt074

Oglesby, D. D., & Mai, P. M. (2012). Fault geometry, rupture dynamics and ground motion from potential earthquakes on the North Anatolian Fault under the Sea of Marmara. *Geophysical Journal International*, *188*(3), 1071–1087. https://doi.org/10.1111/j.1365-246X.2011.05289.x

Stirling, M. W., McVerry, G. H., Gerstenberger, M. C., Litchfield, N. J., van Dissen, R., Berryman, K. R., et al. (2012). National seismic hazard model for New Zealand: 2010 update. *Bulletin of the Seismological Society of America*, *102*(4), 1514–1542. https://doi.org/10.1785/0120110170

Stirling, M. W., Wesnousky, S. G., & Shimazaki, K. (1996). Fault trace complexity, cumulative slip, and the shape of the magnitude-frequency distribution for strike-slip faults: A global survey. *Geophysical Journal International*, *124*(3), 833–868. https://doi.org/10.1111/j.1365-246X.1996.tb05641.x

Townend, J., Sherburn, S., Arnold, R., Boese, C., & Woods, L. (2012). Three-dimensional variations in present-day tectonic stress along the Australia-Pacific plate boundary in New Zealand. *Earth and Planetary Science Letters*, *353*, 47–59.

Uchide, T., Shearer, P. M., & Imanishi, K. (2014). Stress drop variations among small earthquakes before the 2011 Tohoku-oki, Japan, earthquake and implications for the main shock. *Journal of Geophysical Research: Soid Earth*, *119*, 7164–7174. https://doi.org/10.1002/2014JB010943

Wald, D. J., & Heaton, T. H. (1994). Spatial and temporal distribution of slip for the 1992 Landers, California, earthquake. *Bulletin of the Seismological Society of America*, *84*(3), 668–691.

Wang, T., Wei, S. J., Shi, X. H., Qiu, Q., Li, L. L., Peng, D. J., et al. (2018). The 2016 Kaikoura earthquake: Simultaneous rupture of the subduction interface and overlying faults. *Earth and Planetary Science Letters*, *482*, 44–51. https://doi.org/10.1016/j.epsl.2017.10.056

Xu, W. B., Feng, G. C., Meng, L. S., Zhang, A. L., Ampuero, J. P., Burgmann, R., & Fang, L. H. (2018). Transpressional rupture cascade of the 2016 M_w 7.8 Kaikoura earthquake, New Zealand. *Journal of Geophysical Research: Solid Earth*, *123*, 2396–2409. https://doi.org/10.1002/2017JB015168

Geophysical Research Letters

Supporting Information for

Dynamic rupture simulation reproduces spontaneous multi-fault rupture and arrest during the 2016 Mw 7.9 Kaikoura earthquake

Ryosuke Ando[1] and Yoshihiro Kaneko[2]

[1]Department of Earth and Planetary Science, School of Science, University of Tokyo

[2]GNS Science

Contents of this file

Additional Supporting Information (Files uploaded separately)

Movies S1 to S2

Introduction

This supporting information includes the tables of the parameter sets used in this study, supplementary methods and movies showing the spatiotemporal evolution of dynamic rupture propagation in our simulations.

Supplementary methods

Numerical resolution

We use unstructured triangular meshes with the average height of ~710 m, where the faults and the free surface tend to involve relatively smaller and larger triangles due to their irregular and regular shapes, respectively. By random sampling of on-fault grid points, we confirm that the cohesive zone is normally resolved by at least three four elements, which is considered sufficient for BIEM simulations [*Day et al.*, 2005]. As described in[*Day et al.*, 2005], resolving the shrinking of a cohesive zone due to accelerating rupture ensures accurate numerical solutions. We perform the same simulation with two different discretizations and find that the numerical resolutions did not affect our major conclusions. The final slip distribution is independent of two different numerical resolutions that we have tested. Similarly, the rupture nucleation on the Upper Kowhai fault due to dynamic triggering is also almost independent of the numerical resolutions because of its relatively slow process. The rupture arrest is also a relatively slow process, which is not affected by the numerical resolutions.

Numerical method

For the numerical method, we use the Fast Domain Partitioning Boundary Integral Equation Method in a spatio-temporal BIEM framework, which is an efficient $O(N^2)$ and highly accurate numerical scheme [*Ando*, 2016; *Ando et al.*, 2017]. The numerical domain contains 45000 elements and includes fault surfaces and the overlying Earth's surface as a free surface surrounded by the absorbing boundary zones [*Cerjan et al.*, 1985]. The elapsed computation time for each simulation is ~65 minutes with 256 nodes (see table S3 for details).

Table S1. Common model parameters.

Wave speeds		Rigidity	Frictional coefficients		Stress ratios ν*
V_P	V_S (km/s)	(GPa)	Static μ_s	Dynamic μ_d	
5.2	3.0	30	0.35 (0.32**)	0.20	0.66

* $\nu = (\sigma_{hmax} - \sigma_v)/(\sigma_{hmax} - \sigma_{hmin})$
** For Model B (See Table S2)

Table S2. Models with a different set of friction and stress parameters considered in this study.

Model name	μ_s	D_c (m)	Stress ratios σ_{hmin}/σ_v	M_w	Dynamic triggering*
S	0.35	1.0	0.74	7.9	Yes
A	0.35	1.7	0.73	8.0	Yes
B	0.32	0.5	0.76	7.8	Yes
S'	0.35	1.2	0.74	7.5	No
A'	0.35	1.8	0.73	7.6	No
B'	0.35	0.5	0.76	7.4	No

* if No, the rupture extent for all of these cases is limited in the western and eastern Humps fault and the Hundalee fault without triggering the rupture of the Upper Kowhai fault. Except for the dynamic triggering phenomenon, the slip distribution patterns depend very weakly on these parameters, while the overall slip amount increases with increasing the stress drop through decreasing σ_{hmin}/σ_v.

Table S3. Computational cost.

Model size		Computer systems (specifications) and elapsed time	
Number of boundary elements	Time steps	K-computer* (1024 nodes, 8192 cores)	Oakforest-PACS** (256 nodes, 17408 cores)
45000	2000	80 min.	65 min.

* http://www.aics.riken.jp/en/k-computer
** https://www.cc.u-tokyo.ac.jp/system/ofp/index-e.html

Movie S1. Movie of the representative result without the Hope fault and the Papatea fault. (Left) fault slip and (right) the Coulomb Failure Stress ΔCFS. The Kekerengu fault exhibits the maximum slip among the fault area. The rupture is spontaneously arrested at the southwestern end of the western Humps fault and on the northeastern Needles fault. The rupture on the Fidget fault is suppressed by negative ΔCFS due to the slip on the Jordan Thrust.

Movie S2. Fault slip in the case with the Papatea fault and the shallowly dipping Whites fault. (Left) Map view and (right) the view looking down from northeast. The slip on the northern part of the Papatea fault is induced by the rupture of the Jordan Thrust and the Fidget fault, while the rupture propagation to the southern part is limited. The Whites fault is ruptured after the rupture jumps onto the Upper Kowhai fault.

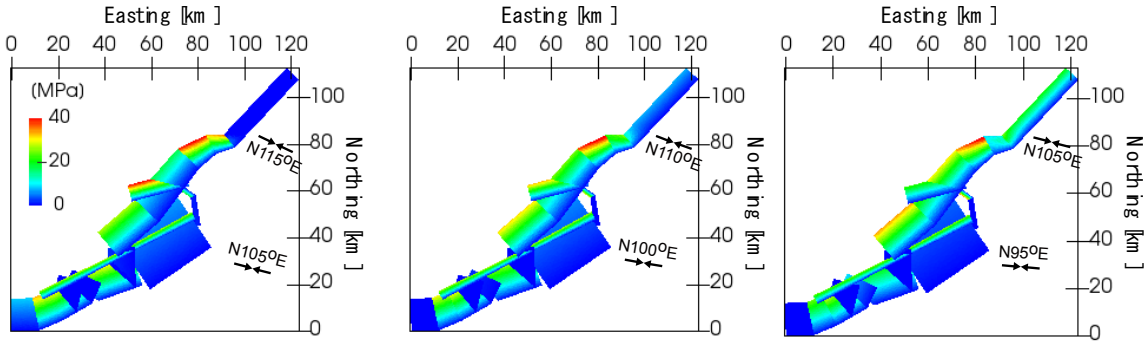

Figure S1. Effect of principal stress axes orientations on the potential stress drop distribution. The maximum principal stress axes are rotated by ±5 degrees (left and right) around the angles of the default Model S (center). The stress ratios and the angular difference between the northern and the central to southern regions are kept unchanged.

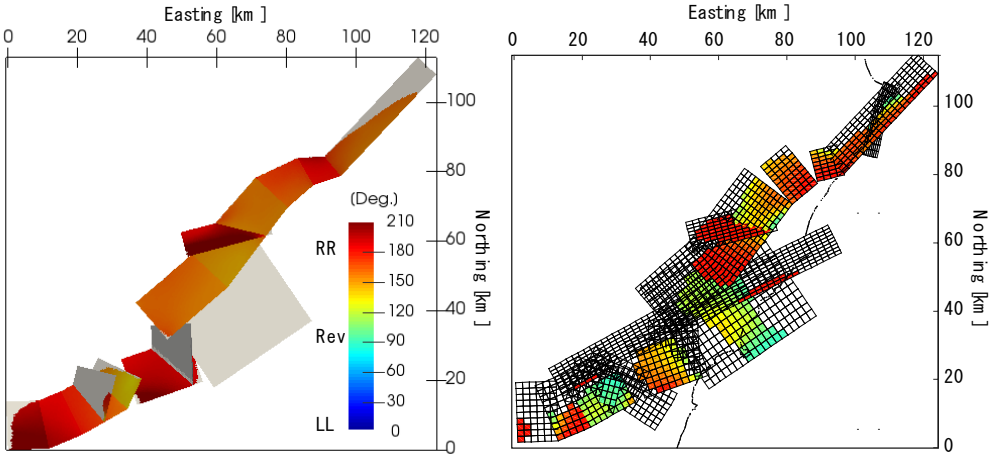

Figure S2. Rake angle distributions in (left) the simulation (Model S) and (right) the source model of Clark et al (2017). In the source model of Clark et al (2017), no color is assigned to fault patches with small slip (<2 m). Slip senses are denoted as LL: left-lateral, Rev: purely reverse and RL: right-lateral.

References

Ando, R. (2016), Fast Domain Partitioning Method for dynamic boundary integral equations applicable to non-planar faults dipping in 3-D elastic half-space, *Geophys. J. Int.*, *207*(2), 833-847, doi:10.1093/gji/ggw299.

Ando, R., K. Imanishi, Y. Panayotopoulos, and T. Kobayashi (2017), Dynamic rupture propagation on geometrically complex fault with along-strike variation of fault maturity: insights from the 2014 Northern Nagano earthquake, *Earth Planets Space*, *69*.

Cerjan, C., D. Kosloff, R. Kosloff, and M. Reshef (1985), A Nonreflecting Boundary-Condition for Discrete Acoustic and Elastic Wave-Equations, *Geophysics*, *50*(4), 705-708, doi:Doi 10.1190/1.1441945.
Day, S. M., L. A. Dalguer, N. Lapusta, and Y. Liu (2005), Comparison of finite difference and boundary integral solutions to three-dimensional spontaneous rupture, *Journal of Geophysical Research: Solid Earth*, *110*(B12), doi:doi:10.1029/2005JB003813.